Nano Research

ISSN 1998-0124 CN 11-5974/O4
https://doi.org/10.26599/NR.2026.94909313

Research Article

Atomic Pd–Br interface for synergistic photocatalytic selective oxidation of alkyl aromatics

Xing Cao[1,2], Tong Han[2], Chen Chen[2], Qing Peng[2](✉), Yadong Li[2](✉)

[1] Institute for Advanced Study and Faculty of Arts and Sciences, Beijing Normal University, Zhuhai 519087, China

[2] Department of Chemistry, Tsinghua University, Beijing 100084, China

Nano Res., **Just Accepted Manuscript** • https://doi.org/10.26599/NR.2026.94909313

https://www.sciopen.com/journal/1998-0124 on Nov. 5, 2026

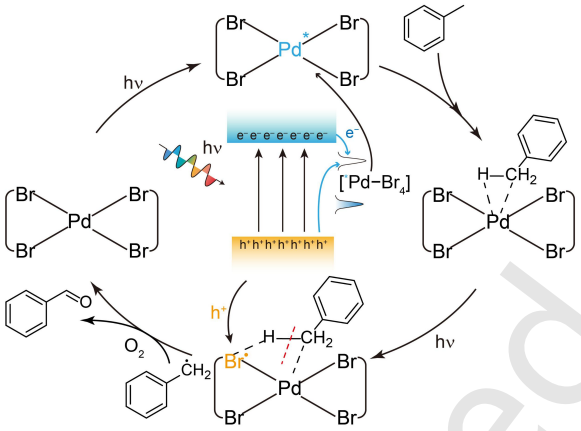
© The Authors(s)

Just Accepted

This is a "Just Accepted" manuscript, which has been examined by the peer-review process and has been accepted for publication. A "Just Accepted" manuscript is published online shortly after its acceptance,which is prior to technical editing and formatting and author proofing. Tsinghua University Press (TUP) provides "Just Accepted" as an optional and free service which allows authors to make their results available to the research community as soon as possible after acceptance. After a manuscript has been technically edited and formatted, and the page proofs have been corrected, it will be removed from the "Just Accepted" web site and published officially with volume and article number (e.g., *Nano Research*, **2025**, *18*, 94906990). Please note that technical editing may introduce minor changes to the manuscript text and/or graphics which may affect the content, and all legal disclaimers that apply to the journal pertain. In no event shall TUP be held responsible for errors or consequences arising from the use of any information contained in these "Just Accepted" manuscripts. To cite this anuscript please use its Digital Object Identifier (DOI®),which is identical for all formats of publication.

Just Accepted

TABLE OF CONTENTS (TOC)



An atomic Pd–Br interface, constructed from single-atom Pd–Br_4 sites on the BiOBr surface, cooperatively activates the benzylic C–H bond of toluene: Br• generated by hole trapping, together with Pd, adsorbs and activates toluene, enabling .selective oxidation under mild conditions

Just Accepted

Research Article

Atomic Pd–Br interface for synergistic photocatalytic selective oxidation of alkyl aromatics

Xing Cao [1,2], Tong Han [2], Chen Chen [2], Qing Peng [2] ✉, Yadong Li [2] ✉

[1] Institute for Advanced Study and Faculty of Arts and Sciences, Beijing Normal University, Zhuhai 519087, China
[2] Department of Chemistry, Tsinghua University, Beijing 100084, China

Received: 9 October 2026; **Revised: 5 November 2026**; **Accepted: 5 November 2026**

✉ Address correspondence to Qing Peng, pengqing@mail.tsinghua.edu.cn; Yadong Li, ydli@mail.tsinghua.edu.cn

Cite this article: *Nano Research*, 2027, 20, 94909313 https://doi.org/10.26599/NR.2026.94909313

ABSTRACT: Photocatalysis offers a mild route to selective hydrocarbon oxidation and is an attractive alternative to harsh thermal oxidation. However, progress in developing efficient catalysts has been slow, largely because the active sites that govern activity and selectivity remain poorly understood. Here, we precisely construct Pd–Br_4 sites on BiOBr nanosheets, creating an atomic Pd–Br interface that captures photogenerated carriers and promotes their separation and utilization. Once a Br atom has trapped a hole, it cooperates with the Pd site to activate the C(sp^3)–H bond of toluene at the atomic interface. The resulting catalyst oxidizes toluene under ambient conditions witha reaction rate of ~3000 μmol g^{-1} h^{-1}(14.9% conversion, >99% benzaldehyde selectivity) , a 48-fold enhancement over the pristine BiOBr supportand $^{-1}$5.4-fold higher than Pd nanoparticles on the same support, with a turnover frequency of 45 h..Under prolonged irradiation, benzoic acid is obtained with 96% selectivity at 98% conversion These findings demonstrate a rational design strategy for single-atom sites in which the atomic Pd–Br interface mediates synergistic C–H bond activation, providing a general route toward efficient heterogeneous photocatalysts.

KEYWORDS: Single-atom site catalyst, synergistic photocatalysis, C–H bond oxidation, Pd active site, atomic interface

Not Accepted

1 Introduction

The selective oxidation of hydrocarbons with molecular oxygen is an ideal way to produce value-added oxygenates [1, 2]. The main obstacle is the intrinsic stability of hydrocarbon C–H bonds, whose high bond dissociation energy (70–130 kcal mol^{-1}) [3] usually requires oxygen activation under elevated temperature and pressure [4]. The exothermic nature of subsequent reaction steps also raises concerns over product selectivity and process safety. By contrast, photogenerated holes carry strong oxidizing power under mild conditions and can therefore activate C–H bonds directly for selective oxidation [5, 6]. However,hotocatalytic phydrocarbon oxidation remains limited by low utilization of photogenerated charge carriers and a scarcity of catalytic sites designed for this demanding reaction [7, 8].

Loading noble metals on semiconductor photocatalysts and forming metal/semiconductor heterojunctions are common strategies to enhance carrier separation and provide reactive sites, thereby improving photocatalytic efficiency [9]. Palladium (Pd) and its alloy nanoparticles are established high-performance catalysts for the thermal catalytic oxidation of toluene and methane [10–12] and have also been used to boost photocatalytic alkane oxidation [13]. Research indicates that low-coordinated edge and corner Pd atoms on the nanoparticles are the primary active sites, cooperating with reactive oxygen species to activate C–H bonds [13, 14]. Consequently, isolated Pd single-atom sites hold significant potential for catalytic activity while maximizing Pd atom utilization [15, 16]. When the metal is reduced to single atoms, the conventional metal/semiconductor Schottky junction disappears, and a distinct catalytic site forms through coordination between the metal and the support, giving an atomically defined interface [17, 18]. This change reshapes interfacial charge-transfer dynamics: it can open new charge-separation pathways, such as interfacial charge transfer (IFCT) [19], and it alters both carrier migration and the fundamental processes that govern substrate activation.

In this work, we constructed a Br-coordinated Pd single-atom site catalyst (Pd_1/BiOBr) on BiOBr nanosheets with surface-exposed Br atoms. These sites serve as new atomic interfaces that facilitate charge transfer between the semiconductor and the metal center, with Pd capturing electrons and Br capturing holes. This process suppresses carrier recombination and activates the site, enabling it to directly activate the benzylic C–H bond of toluene. /BWO_3O_1Unlike our prior study on Pd, where toluene oxidation is driven directly by Pd single atoms trapped holes, the current system features Br-driven C–H bond cleavage , with Pd playing a cooperative role.The photocatalytic toluene oxidation rate over this catalyst reaches ~3000 μmol g^{-1} h^{-1}, 48-fold higher than pristine BiOBr and -fold45.higher than Pd nanoparticles on BiOBr (Pd_{NP}/BiOBr). Mechanistic studies suggest that the Pd–Br_4 site cleaves the benzylic C–H bond through a dual-function mechanism: Pd-

catalyzed toluene adsorption is synergistically coupled with attack by photogenerated holes localized on the coordinated Br atom, forming a carbon radical intermediate that is then selectively oxidized to the desired product.

2 Results and Discussion

The Pd_1/BiOBr single-atom catalyst was synthesized by a coordination anchoring strategy (Fig. 1(a)). Based on our previous work [20], we used low-defect BiOBr nanosheets (diameter ≈ 100 nm, thickness ≈ 10–20 nm, Fig. S1a) that primarily expose (001) facets as the support. The strong affinity between surface Br atoms and Pd^{2+} ions enabled adsorption, followed by thermal anchoring under argon. No new diffraction peaks appeared in the XRD patterns (Fig. S1b), confirming that the BiOBr structure was retained. Analogous catalysts were also prepared on larger BiOBr nanosheets (BiOBr-1) and micrometer-sized plates (BiOBr-2) (Fig. S2). For comparison, Pd nanoparticles supported on BiOBr (Pd_{NP}/BiOBr, 1.0 wt% loading) were prepared by a photo-deposition method.

Scanning transmission electron microscopy (STEM) images of Pd_{NP}/BiOBr showed distinct nanoparticles (yellow circles in Fig. S3), and the corresponding energy-dispersive X-ray spectroscopy (EDS) mapping confirmed that these regions contained aggregated Pd species (Fig. S3b-f). For Pd_1/BiOBr, despite a high Pd loading of 0.71 wt.%, both HRTEM EDS mapping (Fig. S4) and aberration-corrected high-angle annular dark-field STEMEDS mapping (AC HAADF-STEM, Fig. 1b) revealed that Pd was highly dispersed. In the AC HAADF-STEM image of Pd_1/BiOBr (Fig. 1c), the exposed (001) facets showed a well-ordered tetragonal lattice, with bright spots corresponding to Bi atoms in tetragonal BiOBr [21] and no additional bright spots. When the nanosheets were tilted (Fig. 1d), however, numerous anomalous bright spots appeared between the lattice fringes, likely attributable to isolated Pd single atoms. Because Pd has a lower atomic number (Z = 46) than Bi (Z = 83) and the nanosheets are thick, imaging along [001] overlaps the bright Bi atoms, which obscures any intensity-enhanced points.

X-ray photoelectron spectroscopy (XPS) of the Pd 3*d* region (Fig. 1e) distinguished the Pd species in each catalyst.Fo r Pd_{NP}/BiOBr,the spectrum showed Pd $3d_{3/2}$ peaks at 340.4 and 341.8 eV peaks at 335.1 and $3_{5/2}d$and Pd 3 36.5 eV, consistent with metallic Pd^0 with a minor oxidized component In contrast., Pd_1/BiOBr exhibited binding energies between those of Pd^0 and Pd^{2+}, indicating $Pd^{\delta+}$ species [15]. X-ray absorption fine-structure (XAFS) analysis then resolved the Pd oxidation state and local coordination environment in Pd_1/BiOBr. The Pd K-edge X-ray absorption near-edge structure (XANES) spectrum lay between Pd foil and $PdBr_2$ (Fig. 1f), confirming an intermediate oxidation state. The Fourier-transformed extended XAFS (FT-EXAFS) spectrum (Fig. 1g) showed a predominant Pd–Br coordination shell (similar to $PdBr_2$) and no Pd–Pd or Pd–O shells characteristic of Pd foil and PdO, respectively. Fitting of the FT-EXAFS data (Fig. S5, Table S1) reveals a Pd–Br coordination number of 4.1 and an average Pd–Br bond length of 2.44 Å, closely matching the coordination structure of $PdBr_2$. The tetragonal BiOBr surface exposes abundant Br ions, which provide the ligands that anchor Pd into $Pd–Br_4$ single-atom sites (Fig. 1a) [22].

The photocatalytic performance of the catalysts was evaluated using toluene oxidation as the model reaction; the possible products are benzyl alcohol, benzaldehyde, and benzoic acid (Fig. 2a). Under irradiation from an 8 W 400-405 nm LED, Pd_1/BiOBr (20 mg, 0.71 wt% Pd loading) converted 98% of 0.1 mmol toluene within 8 hours, yielding benzoic acid with 96% selectivity (Fig. 2b). Conversion reached 42% within the first hour (91% benzaldehyde selectivity), and prolonged reaction then over-oxidized the benzaldehyde to benzoic acid.

To quantify the toluene activation rate, initial reaction rates were measured under differential reaction conditions (toluene conversion <15%) with 5 mg of catalyst and a 1 h reaction time. The 0.71 wt% Pd_1/BiOBr catalyst achieved an average toluene conversion of 14.9% with >99% selectivity toward benzaldehyde, corresponding to an intrinsic reaction rate of ~3000 μmol g^{-1} h^{-1}. Identical control experiments on Pd_{NP}/BiOBr, pristine BiOBr nanosheets, and $PdBr_2$ gave much lower activities (Fig. 2c). After the Pd single-atom sites were constructed, the toluene oxidation rate was 48-fold higher than pristine BiOBr and 5.4-fold higher than Pd_{NP}/BiOBr. Similar $Pd–Br_4$ sites on larger BiOBr nanosheets and microplates (BiOBr-1 and BiOBr-2) also improved activity by orders of magnitude (Fig. 6*S*), showing that this active-site design is broadly applicable across BiOBr supports of different lateral dimensions.

Turnover frequency (TOF) analysis of toluene oxidation enabled evaluation of Pd catalytic efficiency under varying reaction conditions, revealing a marked difference between the catalysts (Fig. 2d). Pd_{NP}/BiOBr showed a low TOF of 5.9 h^{-1}, whereas the 0.71 wt% Pd_1/BiOBr catalyst reached 45 h^{-1}, close to that reported for state-of-the-art Pd-Au alloy nanoparticle thermal catalysts (~50 h^{-1}) [11]. The comparison is intended only as a benchmark for the order of magnitude of Pd-based activity; the two systems differ in energy input, oxidant pressure and operating temperature.The Pd atom efficiency in Pd_1/BiOBr correlates strongly with dispersion: decreasing the Pd loading raised the TOF progressively, peaking at 78 h^{-1} at 0.3 wt% Pd. The $Pd–Br_4$ site also proved active for substituted arenes, with Pd_1/BiOBr oxidizing various alkyl aromatics (Table 1) and reaching a TOF of 166 h^{-1} for ethylbenzene oxidation.

Apparent quantum yield (AQY) measurements at different incident wavelengths confirmed that the photocatalytic activity of Pd_1/BiOBr is intrinsically linked to the bandgap absorption of BiOBr (Fig. 2e). Quantum yields were appreciable only below 420 nm (AQY ≈ 20% at 405 nm; AQY ≈ 74% at 365 nm). Although Pd_1/BiOBr shows enhanced visible-light absorption through ligand-to-metal charge transfer (LMCT) transitions within the Pd–Br site [23], this absorption produced no photocatalytic activity under visible irradiation. The $Pd–Br_4$ site is therefore photosensitive through LMCT but does not directly drive photocatalytic C–H activation; instead, toluene C–H activation depends on photogenerated holes produced by bandgap excitation of the BiOBr support.

Scavenger experiments established that toluene C–H

Just Accepted

activation requires photogenerated holes rather than electrons or superoxide radicals ($^{\bullet}O_2^-$) derived from electron-driven oxygen reduction (Fig. 3a): quenching holes nearly stopped the reaction, quenching electrons slightly enhanced activity, and quenching $^{\bullet}O_2^-$ had a weaker inhibitory effect. Quenching alkyl radicals markedly suppressed toluene conversion, confirming a radical chain mechanism in which the benzyl radical ($R^{\bullet}$) is a key intermediate. Under strictly anaerobic conditions, activity dropped sharply, and bibenzyl (1,2-diphenylethane, 84% selectivity) became the principal coupling product together with benzyl bromide (10% selectivity). This product distribution supports the radical chain pathway and indicates that oxygen is needed to accept electrons and sustain catalytic turnover. The formation of benzyl bromide further implicates the direct participation of the bromide ligand coordinated to Pd, possibly through C–H oxidative addition followed by reductive elimination. When the atmosphere was replaced with $^{18}O_2$, a substantial amount of ^{18}O- labelled benzaldehyde formed (.Fig7S), demonstrating that the oxygen in benzaldehyde comes mainly from molecular oxygen rather than lattice oxygen.

In situ electron paramagnetic resonance (EPR) spectroscopy usingDMPO as a spin trapreagent monitored radical generation under the same photocatalytic reaction conditions (solvent, substrate concentrations, and catalysts) as the reactivity tests [24]. Spectra recorded after identical irradiation times (Fig. 3b; fitted spectra in Fig. 8S) showed that Pd_1/BiOBr readily generates the DMPO-trapped benzyl radical ($R^{\bullet}$-DMPO adduct) upon illumination, together with a minor $^{\bullet}O_2^-$ signal. By contrast, Pd_{NP}/BiOBr and pristine BiOBr produced much weaker $R^{\bullet}$ signals; their spectra were dominated by oxidized DMPO (DMPOX, septet, Fig. 3b inset) [25] and smaller $^{\bullet}O_2^-$ signals, indicating strong oxidizing power but poor C–H activation.

To probe the toluene oxidation pathway with minimal interference from the strongly polar acetonitrile used in the EPR tests, toluene was instead used as the solvent, and argon purging of the paramagnetic tube reduced dissolved oxygen and suppressed superoxide formation. After 8 minutes of illumination in toluene, the EPR spectra of Pd_1/BiOBr were much better resolved. Spectral simulation confirmed the simultaneous detection of DMPO-adducted $R^{\bullet}$, $^{\bullet}O_2^-$, bromine radical ($Br^{\bullet}$), and $^{\bullet}OH$ (Fig. 9S). Time-resolved EPR showed an initial burst of $Br^{\bullet}$ on irradiation, which decayed as the $R^{\bullet}$ and $^{\bullet}O_2^-$ signals appeared and grew (Fig. 3c). Pd_{NP}/BiOBr also generated a strong $Br^{\bullet}$ signal under the same conditions (Fig. 9S), but this signal stayed dominant with little accompanying $R^{\bullet}$ formation. Because $Br^{\bullet}$ produced by hole oxidation of Br^- can abstract hydrogen from hydrocarbon C–H bonds [26–28], these results suggest that although $Br^{\bullet}$ forms at Br sites on both catalysts, the Pd single-atom sites selectively enable $Br^{\bullet}$-mediated C–H activation of toluene; Pd nanoparticles are much less effective at using the oxidizing power of $Br^{\bullet}$ for substrate activation.

Kinetic isotope effect (KIE) measurements with deuterated toluene showed different values across the catalysts (Figure 10S). Pristine BiOBr showed a KIE of 3.86, a primary isotope effect indicating that C–H bond activation is the rate-determining step (RDS) [29]. Pd_{NP}/BiOBr lowered the KIE to 1.73, showing that Pd nanoparticles facilitate C–H activation and reduce the energy barrier. Pd_1/BiOBr showed an even lower KIE of 1.43; the primary isotope effect is significantly weakened, indicating thatsole rate-determining stepC–H bond cleavage is no longer the . A -mediated hydrogen abstraction, proton and electron transfer processes increasingly contribute to the overall reaction.$^{\bullet}$longside BrThe behavior likely arises from the distinct adsorption configuration of toluene at Pd single-atom sites, which alters the coupling between electron transfer and C–H bond activation.

UPS and UV–vis spectroscopy (Fig. 1S1) showed that, although the bandgap is nearly unchanged, theconduction band minimum (CBM) of Pd_1/BiOBr and Pd_{NP}/BiOBr is upshifted relative to pristine BiOBr, giving photogenerated electrons with higher reducing power for molecular oxygen reduction [30]. The enhanced visible-light absorption transitions ininterbandin these two samples arises from LMCT [23] and Pd nanoparticles [31], respectively.

Steady-state photoluminescence (PL) spectroscopy showed strong suppression of carrier recombination in both Pd_{NP} /and Pd_1/BiOBr, as evidenced by reduced emission intensities (Fig. 2S1). Transient PL measurements revealed divergent dynamics (Fig. 3d): Pd_{NP}/BiOBr showed a shorter fluorescence lifetime because electrons are rapidly extracted through the Schottky junction between the Pd nanoparticle and BiOBr, whereas Pd_1/BiOBr showed the longest lifetime, indicating a different carrier-migration mechanism that keeps excited electrons long-lived. Transient photovoltage (TPV) measurements further supported enhanced charge dynamics in both systems (Fig. 3e), including suppressed electron-hole recombination and prolonged carrier lifetimes. Pd_{NP}/BiOBr produced much larger photovoltage signals, consistent with efficient spatial charge separation at the Schottky junction, whereas the atomically dispersed Pd sites in Pd_1/BiOBr separated charges less efficiently than the Pd nanoparticles.

In situ illuminated XPS of Pd_1/BiOBr supported the charge-trapping mechanism (Fig. 3f): the fraction of higher-valence $Pd^{\delta+}$ species decreased on illumination, indicating electron migration to Pd sites and partial reduction, driven by unoccupied states formed at Pd sites within the BiOBr band gap [32]. Earlier studies showed that incorporating metal d orbitals changes the valence band maximum (VBM) composition of photocatalysts and provides additional active sites [33, 34]. To examine the VBM of Pd_1/BiOBr, partial density of states (PDOS) calculations were performed. As shown in Figure 4a, the Pd–Br_4 site dominates the VBM, indicating that it accumulates photogenerated holes [35]. The CBM is also dominated by the Pd–Br_4 site; the resulting unoccupied states separate photogenerated carriers and enhance their separation. Together with the observed hole trapping by Br^- ions (forming $Br^{\bullet}$), these results indicate that the Pd–Br_4 sites trap both electrons and holes, enhancing charge separation.

A charge density difference analysis was conducted to examine further electron transfer at the Pd–Br_4 interface (Figure 4b). Electrons were found to transfer from BiOBr to the single-atom Pd and from Pd to the coordinating Br atoms, confirming that the single-atom Pd can effectively promote

Not Accepted

local charge transfer. For Pd_{NP}/BiOBr, previous work attributed its beneficial role in toluene photocatalytic oxidation to a Schottky junction formed at the Pd cluster–BiOBr interface that suppresses electron–hole recombination [13]. The charge density difference analysis (Figure 4b) also showed electron accumulation at interfacial Pd sites; moreover, comparing the Fermi levels of Pd_{NP}/BiOBr (−0.30 eV) and BiOBr (−1.11 eV) confirmed a Schottky barrier.

These results well explain the enhanced Br• generation observed by EPR, which shows that both Pd_{NP}- and Pd_1-modification promote hole capture by Br^- ions. However, Pd_{NP}/BiOBr produces abundant Br• but negligible R• radicals, indicating that /$BiOBr_1$it converts toluene far less efficiently than Pd despite efficient charge separation. Consistent with this, photocurrent density measurements (Fig. S11) show that Pd_1/BiOBr outperforms the other catalysts, reflecting its strong surface oxidation activity. Although carrier recombination is suppressed in both Pd_{NP}/BiOBr and Pd_1/BiOBr, the large difference in activity indicates that performance is governed not only by charge-separation efficiency but mainly by the active site and its catalytic mechanism.

To clarify the photocatalytic oxidation mechanism of toluene on the surface of Pd_1/BiOBr and Pd_{NP}/BiOBr (Fig. 31S), a series of DFT calculations was conducted. Based on the structural analyses above, the (001) facet of BiOBr was chosen as the reaction surface, and the adsorption of single-atom Pd coordinated to four Br atoms (Pd_1/BiOBr) and of a Pd cluster (Pd_{NP}/BiOBr) was modeled. To identify the most favorable adsorption configurations, the chemisorption energies of toluene molecules in different orientations on both surfaces were calculated. As shown in Figure 41S, toluene adsorbed vertically at the Pd site of Pd_1/BiOBr was lower in energy than the flat-adsorbed state. For Pd_{NP}/BiOBr, toluene adsorbed at the interface between the Pd cluster and BiOBr was the most stable configuration, with the lowest adsorption energy.

Although both Pd_1/BiOBr and Pd_{NP}/BiOBr are in principle capable of photocatalytic toluene oxidation, Pd_1/BiOBr performed much better experimentally. To understand this difference, we calculated the energy barrier for C–H bond activation at the benzyl group. Figure 4c shows the energy profiles, with the corresponding reaction pathways in the inset. The C–H bond activation barrier for Pd_1/BiOBr (0.33 eV) was much lower than that for Pd_{NP}/BiOBr (0.63 eV). This lower barrier arises from synergistic catalysis by the Pd–Br_4 unit in Pd_1/BiOBr, whereas the analogous active sites in Pd_{NP}/BiOBr are confined to the interface between the Pd cluster and the support.

Building on previous work [13], we propose the following catalytic mechanisms. For Pd_{NP}/BiOBr (Fig. 4d), the Schottky junction at the Pd–BiOBr interface drives charge separation: electrons accumulate on the Pd nanoparticle, and holes concentrate at the interface, where they oxidize toluene to benzaldehyde. When the metal is downsized to single atoms, the Schottky junction disappears and an atomic Pd–Br interface forms (Fig. 4e), which acts as a bifunctional charge-separation center. Under illumination (Fig. 4f), photogenerated electrons transfer to and reduce $Pd^{\delta+}$ (step 1), creating an active site that adsorbs toluene (step 2), while holes oxidize Br^- to Br• radicals (step 3); the resulting benzyl radical is then oxidized by oxygen to benzaldehyde (step 4) [36]. the benzyl radical are provided in the ESM.The subsequent reaction equations for the oxidation of The superior activity of Pd_1/BiOBr over Pd_{NP}/BiOBr therefore arises not only from better Pd atom utilization but from the cooperative Pd–Br dual site that lowers the barrier for C–H cleavage. Comparable cooperative sites in Pd_{NP}/BiOBr exist only at the nanoparticle interface, and their limited number and distinct electronic structure make them far less effective than the uniform Pd–Br_4 single-atom sites described here.

3 Conclusion

In this work, we constructed Pd–Br_4 single-atom sites on BiOBr nanosheets with atomic Pd–Br interfaces. Compared with Pd_{NP}/BiOBr, this design improves both Pd atom utilization and photocatalytic toluene oxidation. The Pd–Br_4 sites capture photogenerated carriers from BiOBr, promoting charge separation and activating the sites themselves. This enables cooperative catalysis at the atomic interface, where the benzylic C–H bond of toluene is adsorbed by the Pd site and cleaved by the Br site, leading to highly efficient photocatalytic oxidation. This study clarifies how carrier separation and active-site function are coupled at single-atom sites during the photocatalytic selective oxidation of alkyl aromatics, and it offers a design guideline for efficient C–H bond activation sites.

4 Experimental

4.1 Synthesis of Pd_1/BiOBr catalyst.

BiOBr nanosheet powder (0.1 g) was dispersed in 9 mL of ultrapure water by ultrasonication. A predetermined volume of a pre-dissolved $Pd(NO_3)_2$ solution (2.5 mg Pd mL^{-1}) was diluted in 1 mL of ultrapure water, and then added dropwise to the above dispersion under stirring in the dark for 4 h. By varying the volume of Pd precursor added (0.4, 0.3, and 0.2 mL), catalysts with different Pd loadings were obtained. After stirring, the product was collected by centrifugation and washed several times with ultrapure water until the supernatant became colorless. The precipitate was then redispersed in 10 mL of ultrapure water by ultrasonication and freeze-dried in the dark. The resulting powder was transferred to a tube furnace and annealed at 150 °C for 2 h under an argon atmosphere with a heating rate of 2 °C min^{-1}, yielding the final Pd_1/BiOBr catalysts. ICP- OES confirmed the Pd loadings to be 0.71, 0.56, and 0.30 wt%, respectively.

4.2 *In situ* EPR experiments

In situ EPR measurements under simulated catalytic conditions: catalyst (5 mg) was dispersed in 3 mL of acetonitrile, then 0.1 mmol of toluene was added, and the mixture was ultrasonicated. Subsequently, 12.4 μL of DMPO was added to 1 mL of the above solution, mixed thoroughly, and transferred to an EPR tube. EPR spectra were recorded under illumination using a 300 W Xe lamp.

In situ EPR measurements under toluene solvent conditions: catalyst (2 mg) was dispersed in 1 mL of toluene,

Just Accepted

and 12.4 μL of DMPO was added. The mixture was transferred to an EPR tube, and argon was bubbled through the solution to displace air. EPR spectra were then recorded under a 300 W Xe lamp illumination.

Electronic Supplementary Material: Supplementary material (Figures S1–S14 and Table S1) is available in the online version of this article at https://doi.org/10.26599/NR.2026.94909313.

Data availability

All data needed to support the conclusions in the paper are presented in the manuscript and the Electronic Supplementary Material. Additional data related to this paper may be requested from the corresponding author.

Acknowledgements

This work was financially supported by the National Natural Science Foundation of China (Nos. 22275109, 22509161) ,the Fundamental Research Center of Single-Atom Catalysis (No. 22388102),and)2263300003 (No. the Fundamental Research Funds for the Central Universities.

Declaration of competing interest

Yadong Li is the **editor-in-chief** of this journal, but he is not involved in the peer-review or decision of this article.

Author contribution statement

Q.P. and Y.D. L. supervised the research, acquired funding, and revised the manuscript. X.C. designed experiments, optimized catalysts, performed material characterizations, and wrote the manuscript. T.H. conducted HRTEM tests, catalysis testing, and manuscript revision. C.C. provided advice and contributed to scientific discussions throughout the project.

Use of AI statement

None.

References

[1] H. Tateno, S. Iguchi, Y. Miseki, K. Sayama, Photo-Electrochemical C–H Bond Activation of Cyclohexane Using a WO_3 Photoanode and Visible Light, *Angew. Chem. Int. Ed.* **2018**, *57* (35), 11238–11241.

[2] G. Laudadio, Y. Deng, K. van der Wal, D. Ravelli, M. Nuno, M. Fagnoni, D. Guthrie, Y. Sun, T. Noel, C(sp^3)–H functionalizations of light hydrocarbons using decatungstate photocatalysis in flow, *Science* **2020**, *369* (6499), 92–96.

[3] C. Xu, Y. Pan, G. Wan, H. Liu, L. Wang, H. Zhou, S.-H. Yu, H.-L. Jiang, Turning on visible-light photocatalytic C-H oxidation over metal–organic frameworks by introducing metal-to-cluster charge transfer, *J. Am. Chem. Soc.* **2019**, *141* (48), 19111–19117.

[4] H. Sterckx, B. Morel, B. U. W. Maes, Catalytic aerobic oxidation of C(sp^3)–H bonds, *Angew. Chem. Int. Ed.* **2019**, *58* (24), 7946–7970.

[5] Y. Jiang, S. Li, X. Fan, Z. Tang, Recent advances on aerobic photocatalytic methane conversion under mild conditions, *Nano Res.* **2023**, *16* (11), 12558–12571.

[6] S. Tian, J. Li, B. Wang, X. Wang, X. Hu, H. Wang, L. Chen, S.-F. Yin, Water enhances photocatalytic activity for toluene selective oxidation in acetic acid solution, *Nano Res.* **2025**, *18* (3), 94907206.

[7] Y. Shi, P. Li, H. Chen, Z. Wang, Y. Song, Y. Tang, S. Lin, Z. Yu, L. Wu, J. C. Yu, X. Fu, Photocatalytic toluene oxidation with nickel-mediated cascaded active units over Ni/Bi_2WO_6 monolayers, *Nat. Commun.* **2024**, *15* (1), 4641.

[8] X. Liu, S. Huang, R. S. H. Khoo, L. Huang, W. Zhu, L. Wang, Selective photocatalytic C—H oxidation using all-inorganic perovskite quantum dots encapsulated in UiO-series MOFs, *Small Methods* **2025**, 2401910.

[9] Y. Dai, C. Poidevin, C. Ochoa-Hernandez, A. A. Auer, H. Tuysuz, A Supported Bismuth Halide Perovskite Photocatalyst for Selective Aliphatic and Aromatic C–H Bond Activation, *Angew. Chem. Int. Ed.* **2020**, *59* (14), 5788–5796.

[10] N. Agarwal, S. J. Freakley, R. U. McVicker, S. M. Althahban, N. Dimitratos, Q. He, D. J. Morgan, R. L. Jenkins, D. J. Willock, S. H. Taylor, C. J. Kiely, G. J. Hutchings, Aqueous Au-Pd colloids catalyze selective CH_4 oxidation to CH_3OH with O_2 under mild conditions, *Science* **2017**, *358* (6360), 223–227.

[11] L. Kesavan, R. Tiruvalam, M. H. Ab Rahim, M. I. bin Saiman, D. I. Enache, R. L. Jenkins, N. Dimitratos, J. A. Lopez-Sanchez, S. H. Taylor, D. W. Knight, C. J. Kiely, G. J. Hutchings, Solvent-free oxidation of primary carbon-hydrogen bonds in toluene using Au-Pd alloy nanoparticles, *Science* **2011**, *331* (6014), 195–199.

[12] P. Zhang, Y. Gong, H. Li, Z. Chen, Y. Wang, Solvent-free aerobic oxidation of hydrocarbons and alcohols with Pd@N-doped carbon from glucose, *Nat. Commun.* **2013**, *4* (1), 1593.

[13] X. Li, T. Wang, X. Tao, G. Qiu, C. Li, B. Li, Interfacial synergy of Pd sites and defective BiOBr for promoting the solar-driven selective oxidation of toluene, *J. Mater. Chem. A* **2020**, *8* (34), 17657–17669.

[14] S. Okunaka, Y. Hitomi, H. Tokudome, Boosting the visible-light-induced toluene oxidation via synergistic effect between nanoparticulate Pd/$BiVO_4$ photocatalyst and a cyclic nitroxyl redox mediator, *J. Catal.* **2022**, *414*, 137–142.

[15] R. Sun, X. Cao, J. Ma, H.-C. Chen, C. Chen, Q. Peng, Y. Li, Regulation of Pd single-atom coordination for enhanced photocatalytic oxidation of toluene to benzaldehyde, *Nat. Synth.* **2025**, *4* (8), 965–975.

[16] K. Sun, X. Pei, S. Wang, X. Wang, P. Qiao, D. Wang, L. Liu, J. Ye, H. Song, Synergistic enhancement of electron and hole transport by Pd single atoms and gradient-distributed Ti^{3+} species for high-performance photocatalytic oxidation of CH_4 to oxygenates, *Angew. Chem. Int. Ed.* **2025**, *64* (49), e202517585.

[17] Y. Chen, S. Ji, W. Sun, Y. Lei, Q. Wang, A. Li, W. Chen, G. Zhou, Z. Zhang, Y. Wang, L. Zheng, Q. Zhang, L. Gu, X. Han, D. Wang, Y. Li, Engineering the Atomic Interface with Single Platinum Atoms for Enhanced Photocatalytic Hydrogen Production, *Angew. Chem. Int. Ed.* **2020**, *59* (3), 1295–1301.

[18] B. Wang, H. R. Cai, S. H. Shen, Single Metal Atom Photocatalysis, *Small Methods* **2019**, *3* (9), 1800447.

[19] X. Ye, Y. Li, P. Luo, B. He, X. Cao, T. Lu, Iron sites on defective BiOBr nanosheets: Tailoring the molecular oxygen activation for enhanced photocatalytic organic synthesis, *Nano Res.* **2021**, *15* (2), 1509–1516.

[20] X. Cao, A. Huang, C. Liang, H.-C. Chen, T. Han, R. Lin, Q. Peng, Z. Zhuang, R. Shen, H. M. Chen, Y. Yu, C. Chen, Y. Li, Engineering lattice disorder on a photocatalyst: photochromic BiOBr nanosheets enhance activation of aromatic C–H bonds via water oxidation, *J. Am. Chem. Soc.* **2022**, *144* (8), 3386–3397.

[21] T. Han, X. Cao, H. Chen, J. Ma, Y. Yu, Y. Li, W. Xu, K. Sun, A. Huang, Z. Chen, C. Chen, H. Zhang, B. Ye, Q. Peng, Y. Li, Photosynthesis of Benzonitriles on BiOBr Nanosheets Promoted by Vacancy Associates, *Angew. Chem. Int. Ed.* **2023**, *62* (49), e202313325.

[22] G. Zhou, B. Lei, F. Dong, Lewis Acid Sites in (110) Facet-Exposed BiOBr Promote C–H Activation and Selective Photocatalytic Toluene Oxidation, *ACS Catal.* **2024**, (7), *144*791–4798.

Just Accepted

[23] C. Creutz, B. S. Brunschwig, N. Sutin, Interfacial charge-transfer absorption: 3. Application to semiconductor-molecule assemblies, *J. Phys. Chem. B* **2006**, *110* (50), 25181–25190.

[24] Z. Yu, Z. Chen, Y. Chen, Q. Peng, R. Lin, Y. Wang, R. Shen, X. Cao, Z. Zhuang, Y. Li, Photocatalytic hydrogenation of nitroarenes using $Cu_{1.94}S$-$Zn_{0.23}Cd_{0.77}S$ heteronanorods, *Nano Res.* **2018**, *11* (7), 3730–3738.

[25] H. A. O. Hill, P. J. Thornalley, The oxidative ring opening of the cyclic nitrone spin trap 5, 5-dimethyl-1-pyrroline-1-oxide (DMPO): free radical involvment, *Inorg. Chim. Acta* **1982**, *67* L35–L36.

[26] R. Yuan, S. Fan, H. Zhou, Z. Ding, S. Lin, Z. Li, Z. Zhang, C. Xu, L. Wu, X. Wang, X. Fu, Chlorine-radical-mediated photocatalytic activation of C–H bonds with visible light, *Angew. Chem. Int. Ed.* **2013**, *52* (3), 1035–9.

[27] T. Kawasaki, N. Ishida, M. Murakami, Dehydrogenative coupling of benzylic and aldehydic C–H bonds, *J. Am. Chem. Soc.* **2020**, *142* (7), 3366–3370.

[28] Z. Li, L. Luo, M. Li, W. Chen, Y. Liu, J. Yang, S. M. Xu, H. Zhou, L. Ma, M. Xu, X. Kong, H. Duan, Photoelectrocatalytic C–H halogenation over an oxygen vacancy-rich TiO_2 photoanode, *Nat. Commun.* **2021**, *12* (1), 6698.

[29] Y. M. Kwon, Y. Lee, G. E. Evenson, T. A. Jackson, D. Wang, Crystal structure and C–H bond-cleaving reactivity of a mononuclear Co^{IV} – dinitrate complex, *J. Am. Chem. Soc.* **2020**, *142* (31), 13435–13441.

[30] M. Guan, C. Xiao, J. Zhang, S. Fan, R. An, Q. Cheng, J. Xie, M. Zhou, B. Ye, Y. Xie, Vacancy associates promoting solar-driven photocatalytic activity of ultrathin bismuth oxychloride nanosheets, *J. Am. Chem. Soc.* **2013**, *135* (28), 10411–10417.

[31] H. Song, X. Meng, Z. Wang, Z. Wang, H. Chen, Y. Weng, F. Ichihara, M. Oshikiri, T. Kako, J. Ye, Visible-Light-Mediated Methane Activation for Steam Methane Reforming under Mild Conditions: A Case Study of Rh/TiO_2 Catalysts, *ACS Catal.* **2018**, *8* (8), 7556–7565.

[32] H. Irie, S. Miura, K. Kamiya, K. Hashimoto, Efficient visible light-sensitive photocatalysts: Grafting Cu(II) ions onto TiO_2 and WO_3 photocatalysts, *Chem. Phys. Lett.* **2008**, *457* (1–3), 202–205.

[33] P. Murugan, V. Kumar, Y. Kawazoe, Thickness dependence of the atomic and electronic structures of TiO_2 rutile (110) slabs and the effects on the electronic and magnetic properties of supported clusters of Pd and Rh, *Phys. Rev. B* **2006**, *73* (7), 75401.

[34] E. Mete, O. Gülseren, Ş. Ellialtıoğlu, Modification of TiO_2 (001) surface electronic structure by Au impurity investigated with density functional theory, *Phys. Rev. B* **2009**, *80* (3), 35422.

[35] W. Zhang, C. Fu, J. Low, D. Duan, J. Ma, W. Jiang, Y. Chen, H. Liu, Z. Qi, R. Long, Y. Yao, X. Li, H. Zhang, Z. Liu, J. Yang, Z. Zou, Y. Xiong, High-performance photocatalytic nonoxidative conversion of methane to ethane and hydrogen by heteroatoms-engineered TiO_2, *Nat. Commun.* **2022**, *13* (1), 2806.

[36] X. Cao, Z. Chen, R. Lin, W.-C. Cheong, S. Liu, J. Zhang, Q. Peng, C. Chen, T. Han, X. Tong, Y. Wang, R. Shen, W. Zhu, D. Wang, Y. Li, A photochromic composite with enhanced carrier separation for the photocatalytic activation of benzylic C–H bonds in toluene, *Nat. Catal.* **2018**, *1* (9), 704–710.

Just Accepted

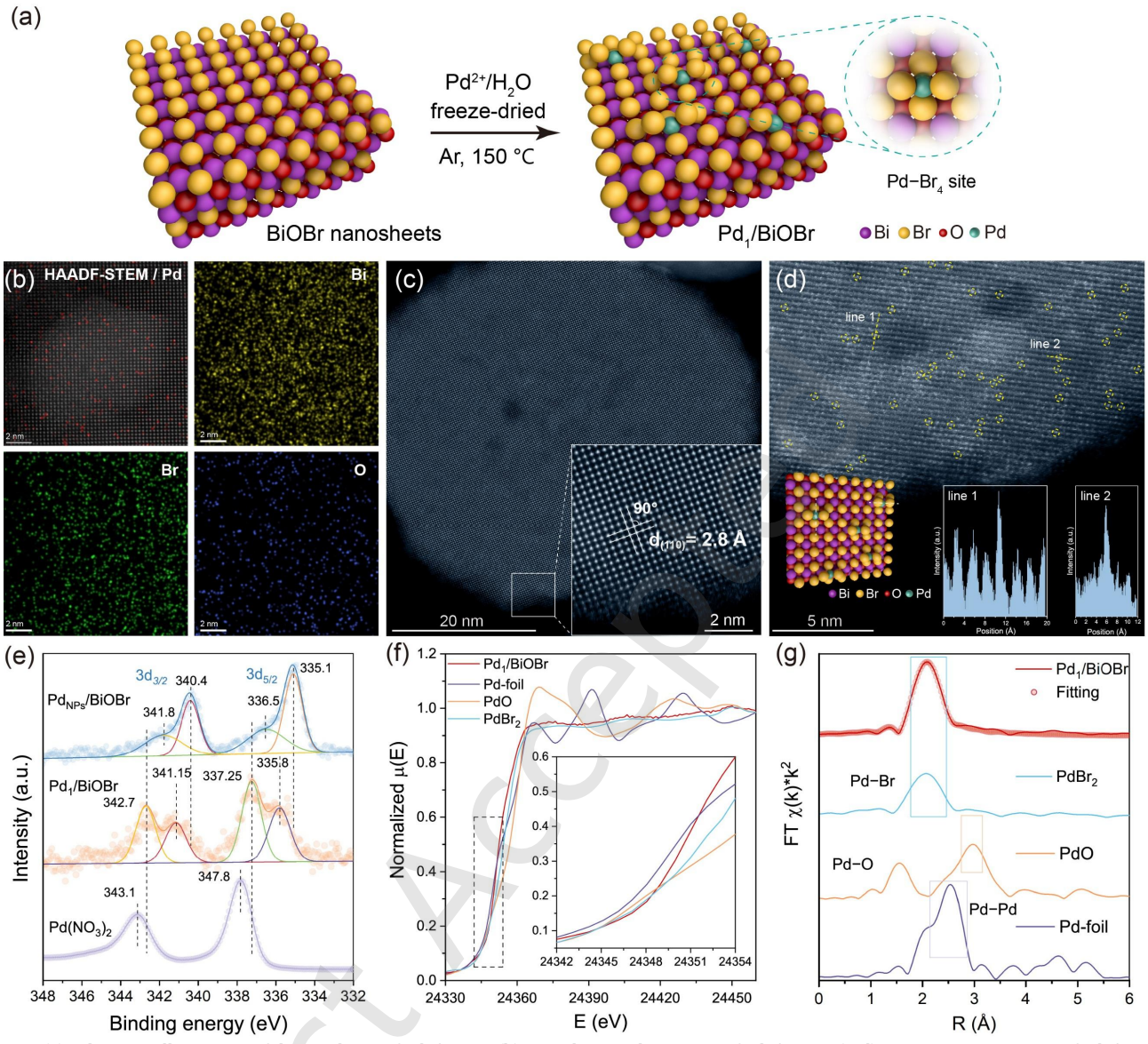


Figure 1 (a) Schematic illustration of the synthesis of Pd_1/BiOBr. (b) EDS elemental mapping of Pd_1/BiOBr. (c, d) HAADF-STEM images of Pd_1/BiOBr. (e) XPS spectra of Pd_1/BiOBr, Pd_{NP}/BiOBr, and $Pd(NO_3)_2$. (f, g) Pd K-edge XANES spectra and Fourier-transformed k^2-weighted Pd K-edge EXAFS spectra of Pd_1/BiOBr and referencesrespectively, .

Just Accepted

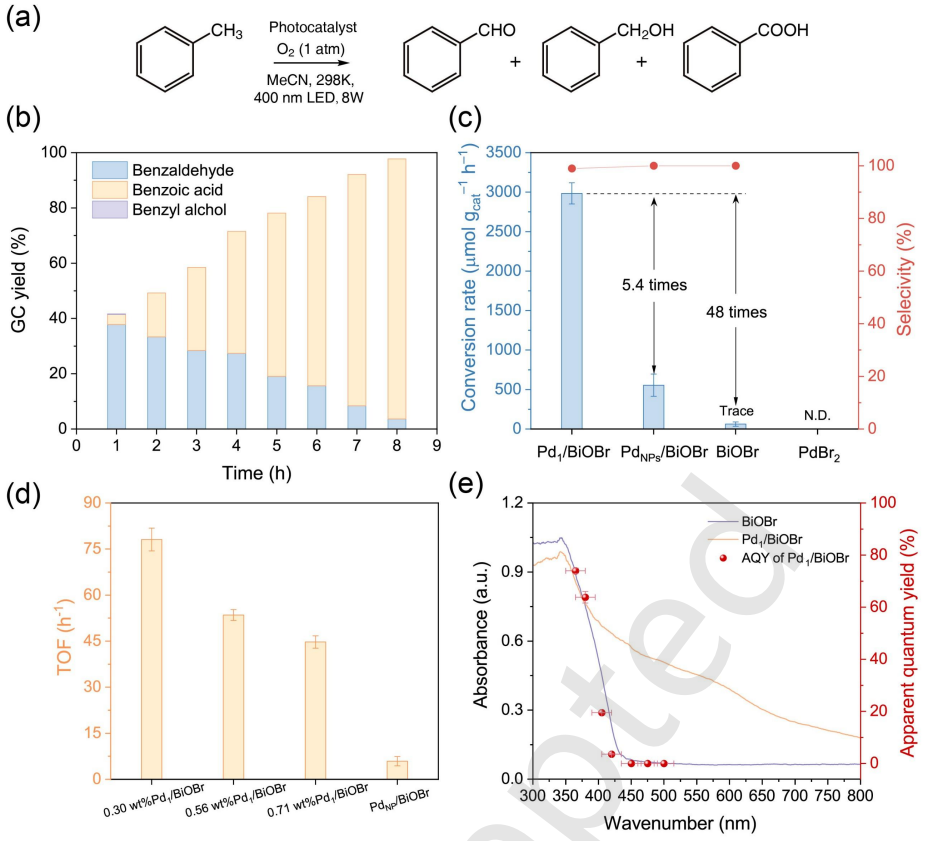


Figure 2 (a) Schematic illustration of photocatalytic toluene oxidation. (b) Time-dependent product yields during toluene oxidation over Pd_1/BiOBr. (c) Photocatalytic toluene oxidation performance over various samples. (d) Comparison of TOF for toluene oxidation over Pd_1/BiOBr and Pd_{NP}/BiOBr catalysts with different Pd loadings. (e) UV–vis diffuse reflectance spectra of BiOBr and Pd_1/BiOBr, together with the AQY of Pd_1/BiOBr under LED irradiation at different wavelengths.

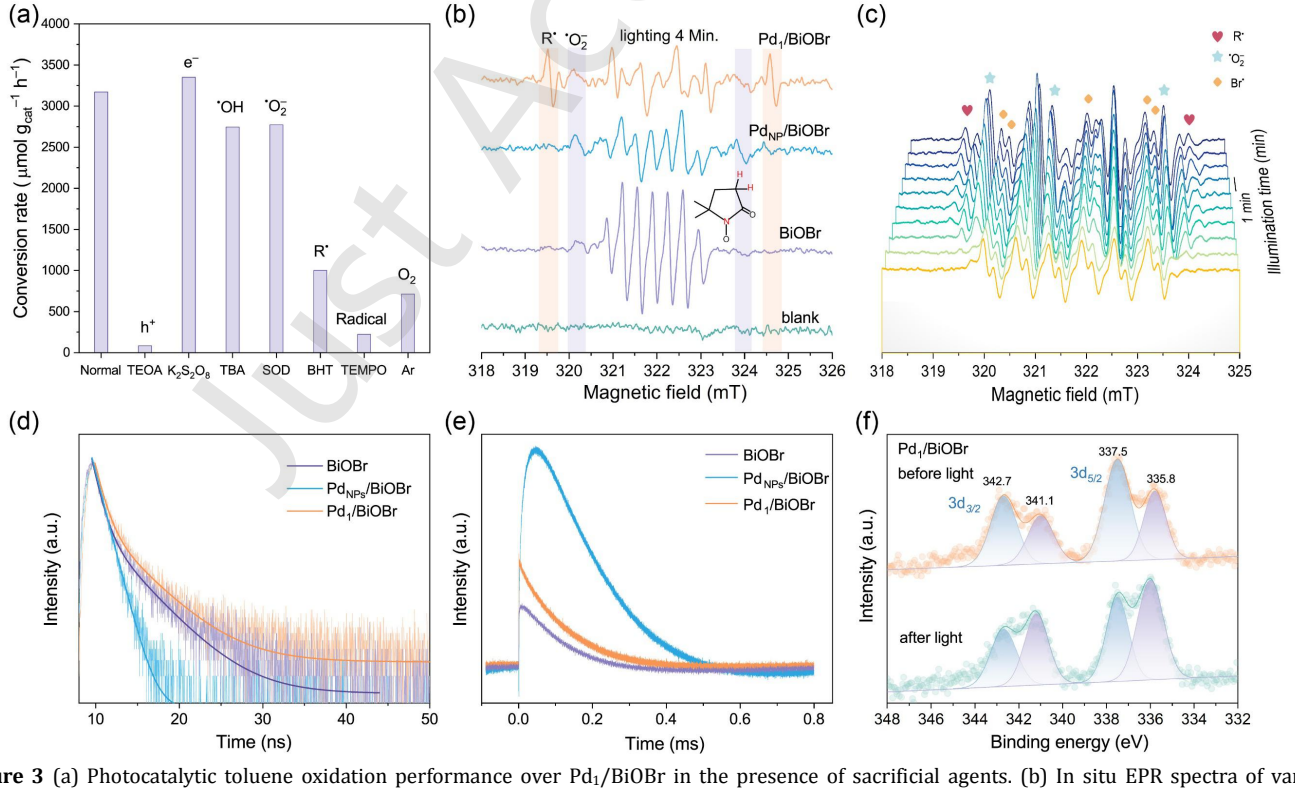


Figure 3 (a) Photocatalytic toluene oxidation performance over Pd_1/BiOBr in the presence of sacrificial agents. (b) In situ EPR spectra of various samples under photocatalytic conditions. (c) In situ EPR spectra of Pd_1/BiOBr in toluene solvent at different irradiation times. (d) Transient PL spectra and (e) TPV responses of various samples. (f) XPS spectra of Pd_1/BiOBr before and after light irradiation.

Just Accepted

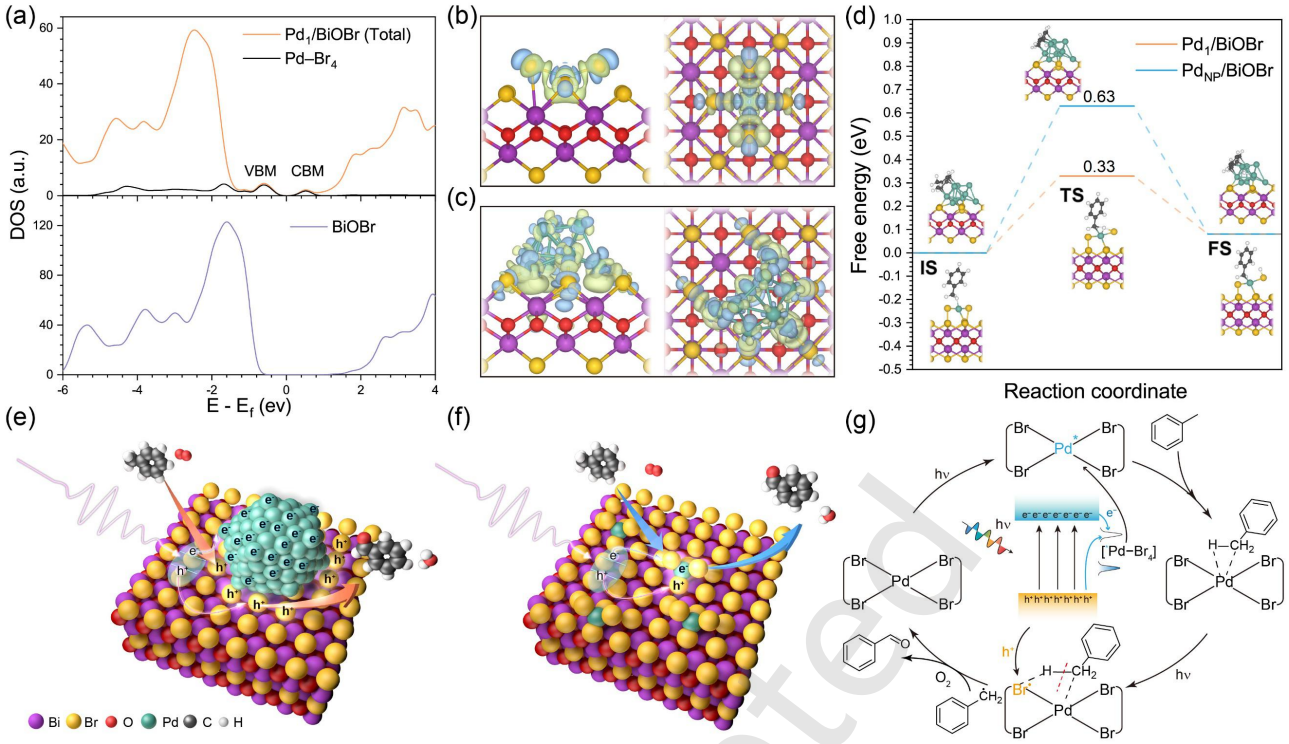
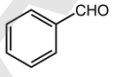
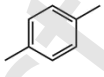
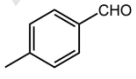
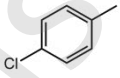
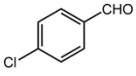
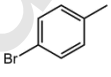
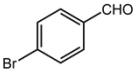
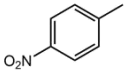
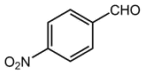
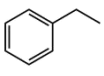
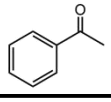


Figure 4 (a) DOS for the total system and the Pd–Br_4 unit in Pd_1/BiOBr. (b) Charge density difference plots of Pd_1/BiOBr: top view (3D plot, upper) and side view (lower). The isosurface level is set to 0.003 e $Å^{-3}$; cyan and yellow represent charge depletion and accumulation, respectively. Atom colors: Bi (purple), Pd (green), Br (yellow), C (gray), O (red), H (white). (c) Gibbs free energy diagram for C–H bond activation of toluene on Pd_1/BiOBr and Pd_{NP}/BiOBr surfaces. IS, initial state; TS, transition state; FS, final state. Inset: optimized structures for the C–H bond activation step (Pd_1/BiOBr top, Pd_{NP}/BiOBr bottom). (d–f) Schematic illustrations of (d) Pd nanoparticle and (e) Pd single atom on BiOBr surface, and (f) catalytic mechanism of toluene oxidation at the Pd–Br_4 site.

Table 1. Catalytic performance of Pd_1/BiOBr for the oxidation of substituted aromatics

Entry	Substrate	Product	Selectivity (%)	TOF (h^{-1})
1			>99	45
2			98	83
3			>99	54
4			>99	55
5			>99	28
6			96	166

Reaction conditions: atmosphere, 8 W $_2$alkyl aromatics (0.1 mmol), photocatalyst (5 mg), anhydrous acetonitrile (3 mL), O400-.405 nm LED, 25 ± 0.5 °C, 1 h

Just Accepted

© The Author(s) 20xx. *Nano Research* published by Tsinghua University Press. The articles published in this open access journal are distributed under the terms of the Creative Commons Attribution 4.0 International License (http://creativecommons.org/licenses/by/4.0/), which permits use, distribution and reproduction in any medium, provided the original work is properly cited.

Electronic Supplementary Material

Atomic Pd–Br interface for synergistic photocatalytic selective oxidation of alkyl aromatics

Xing Cao [1,2], Tong Han [2], Chen Chen [2], Qing Peng [2] ✉, Yadong Li [2] ✉

[1] Institute for Advanced Study and Faculty of Arts and Sciences, Beijing Normal University, Zhuhai 519087, China
[2] Department of Chemistry, Tsinghua University, Beijing 100084, China

Supporting information to https://doi.org/10.26599/NR.2026.94909313

Just Accepted

Address correspondence to Qing Peng, pengqing@mail.tsinghua.edu.cn; Yadong Li, ydli@mail.tsinghua.edu.cn

Table S1 EXAFS fitting results of Pd_1/BiOBr and $PdBr_2$

Sample	Path	CN	*R* (Å)	σ^2 (10^{-3} Å^2)	ΔE_0 (eV)	R factor
Pd_1/BiOBr	Pd–Br	4.1±0.14	2.44±0.002	4.2±0.2	7.4±0.5	0.001
$PdBr_2$	Pd–Br	4.0±0.13	2.43±0.007	5.7±1.0	6.0±1.5	0.004

CN, the coordination number of Pd; R, the bond length; ΔE_0, the inner potential correction.

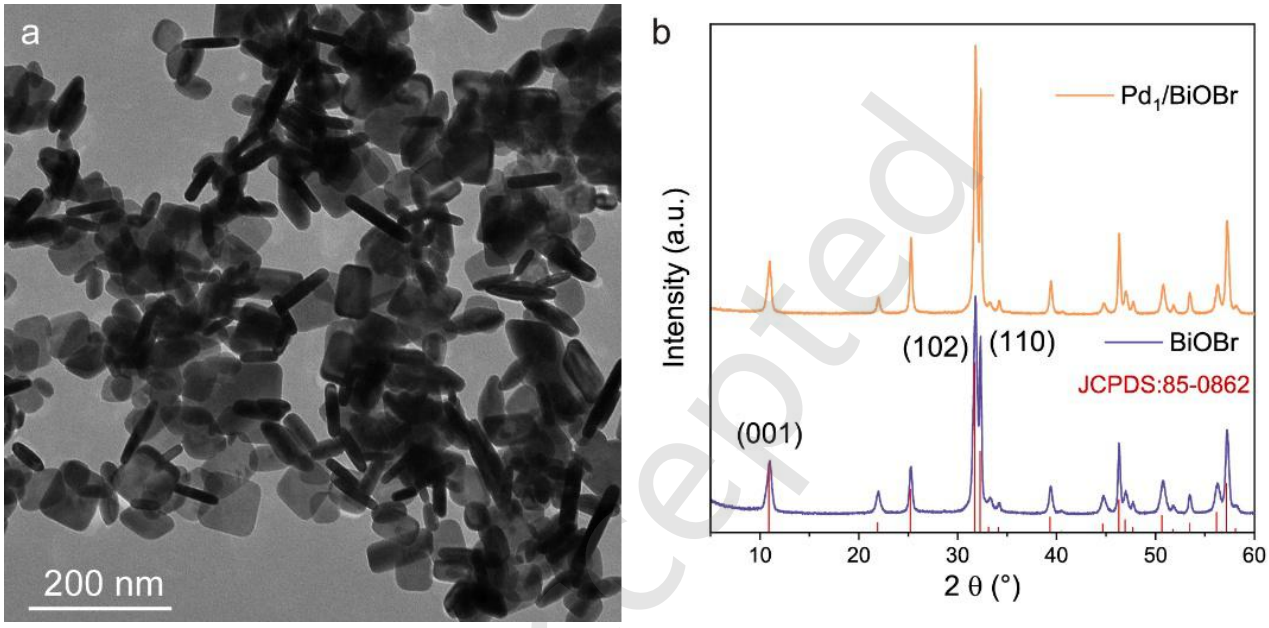


Figure S1 (a) BiOBr nanosheets; (b) XRD patterns of BiOBr nanosheets and Pd_1/BiOBr nanosheets.

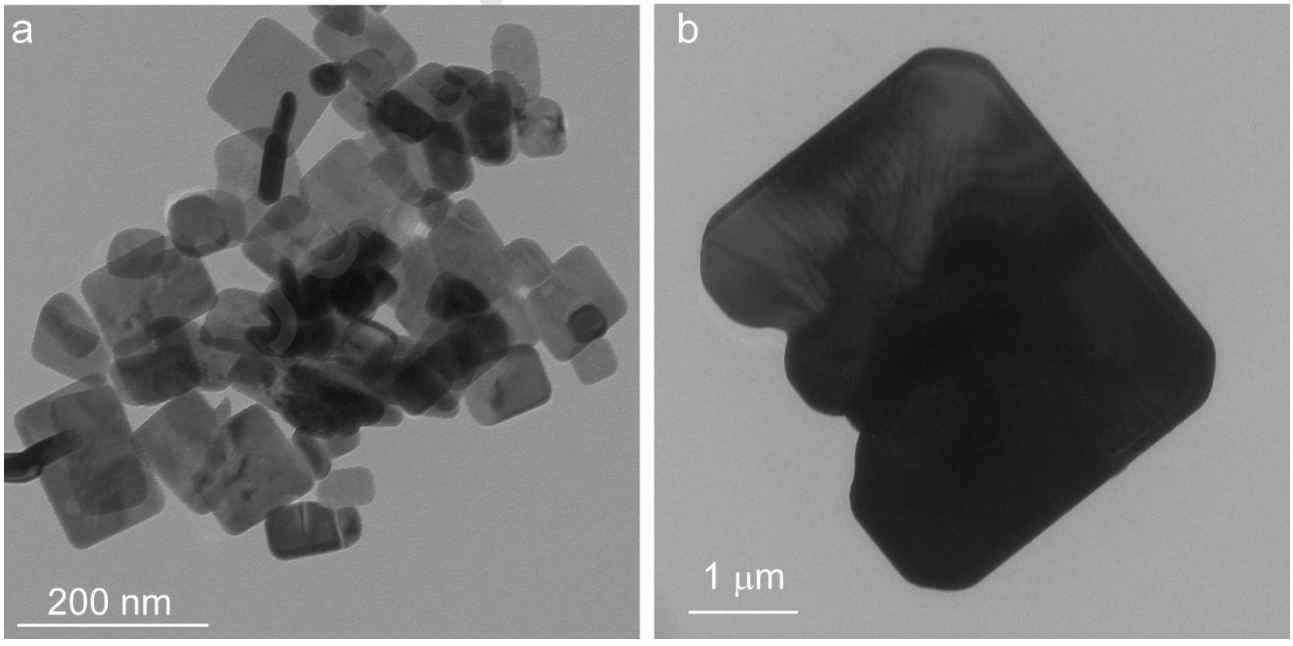


Figure S2 (a) TEM image of BiOBr-1 nanosheets; (b) TEM image of BiOBr-2 micro-sheets.

Accepted

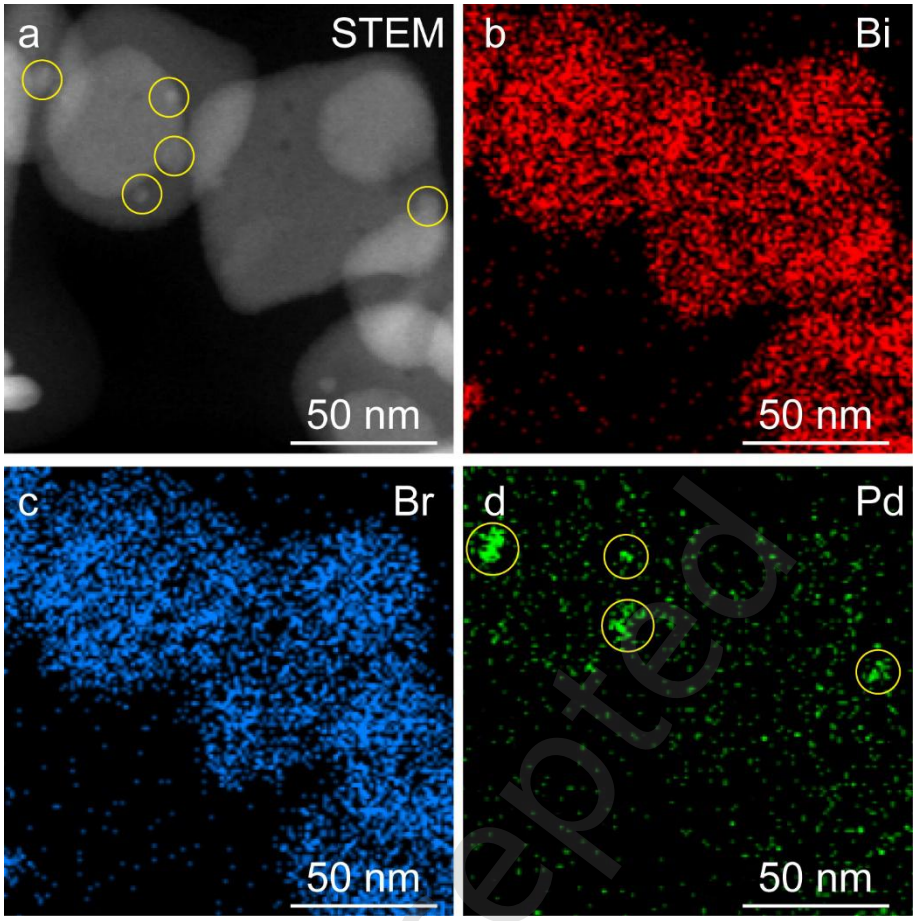


Figure S3 STEM and EDS mapping of Pd_{NP}/BiOBr.

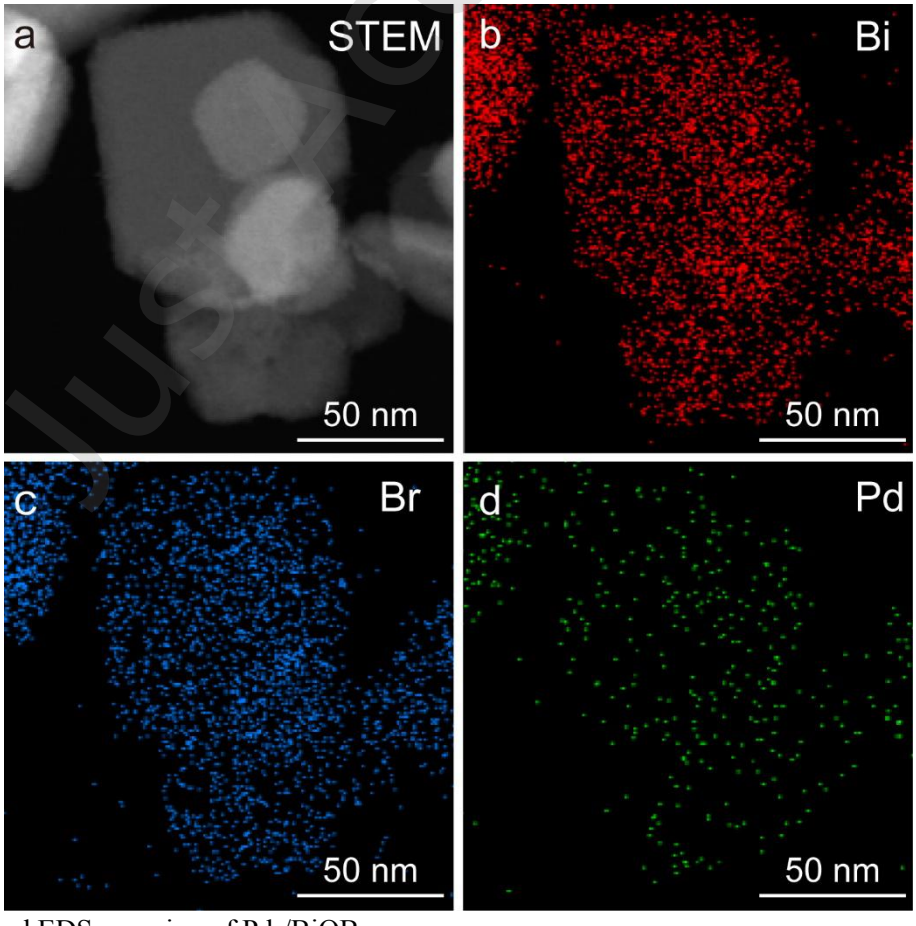


Figure S4 STEM and EDS mapping of Pd_1/BiOBr.

Just Accepted

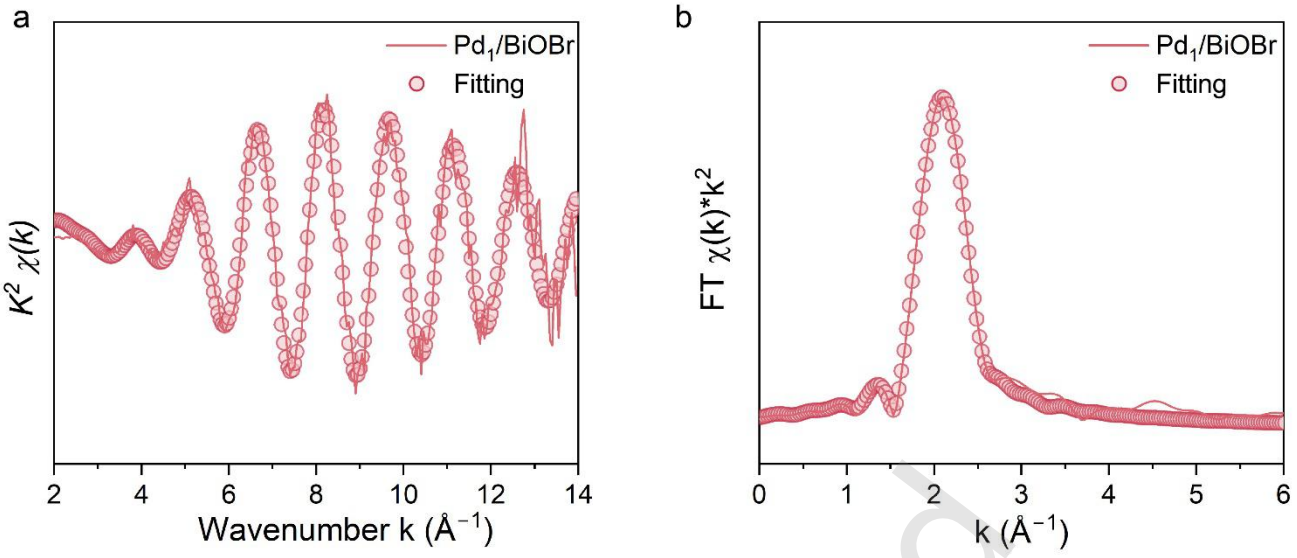


Figure S5 The EXAFS fitting results of Pd_1/BiOBr: (a) K-space, (b) R-space.

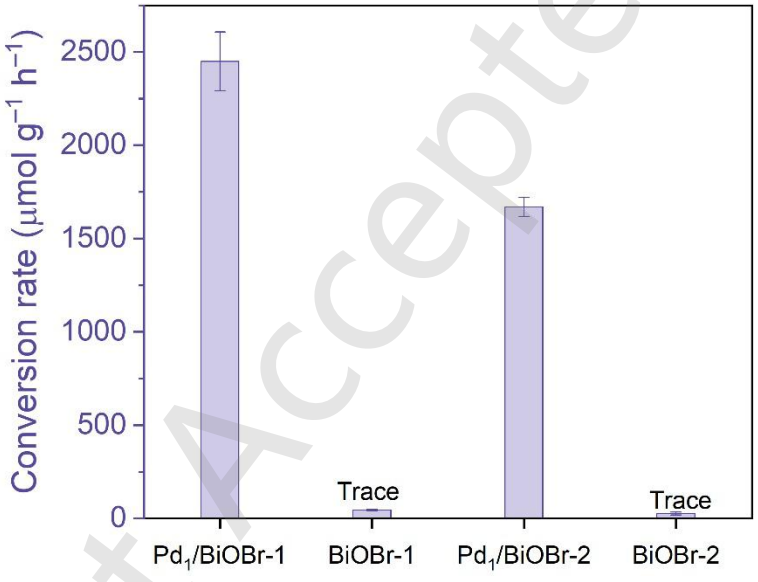


Figure S6 Photocatalytic toluene oxidation performance over different BiOBr supports and their Pd single-atom site-modified catalysts.

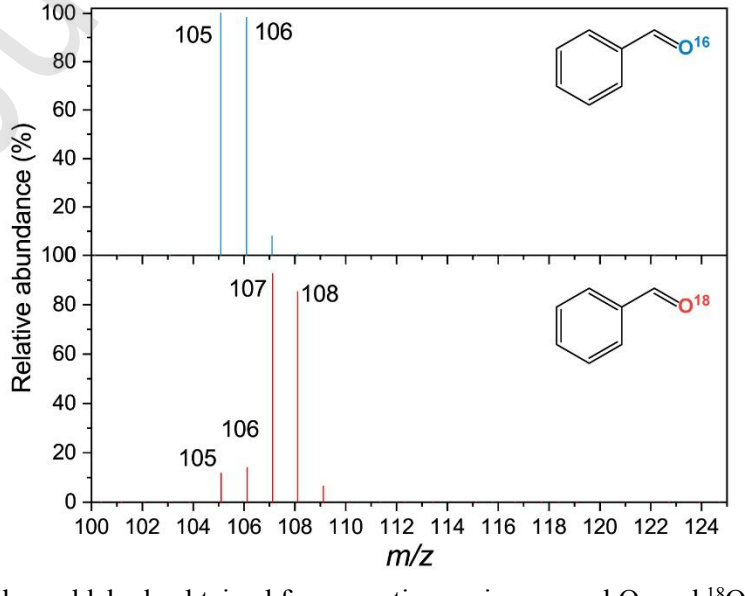


Figure S7 Mass spectra of benzaldehyde obtained from reactions using normal O_2 and $^{18}O_2$ were compared.

Just Accepted

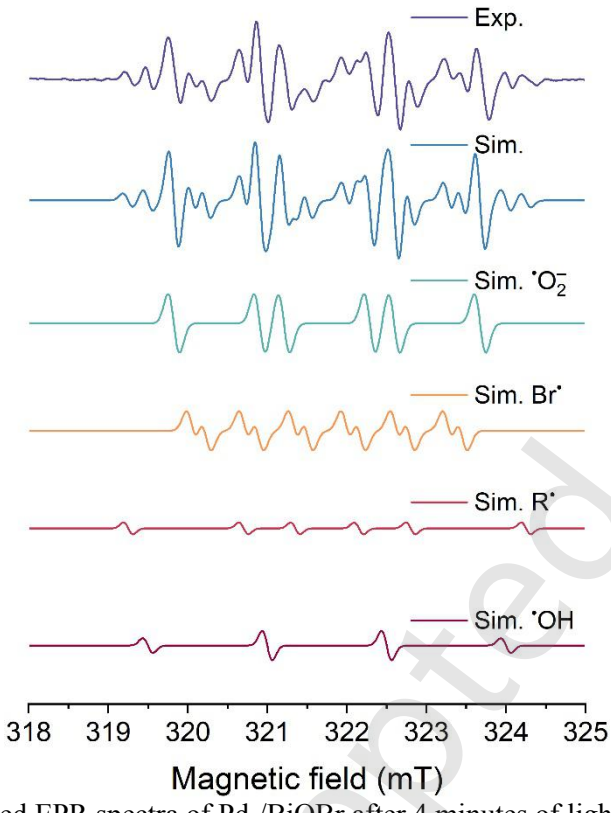


Figure S8 Experimental and fitted EPR spectra of Pd_1/BiOBr after 4 minutes of light irradiation in acetonitrile solvent.

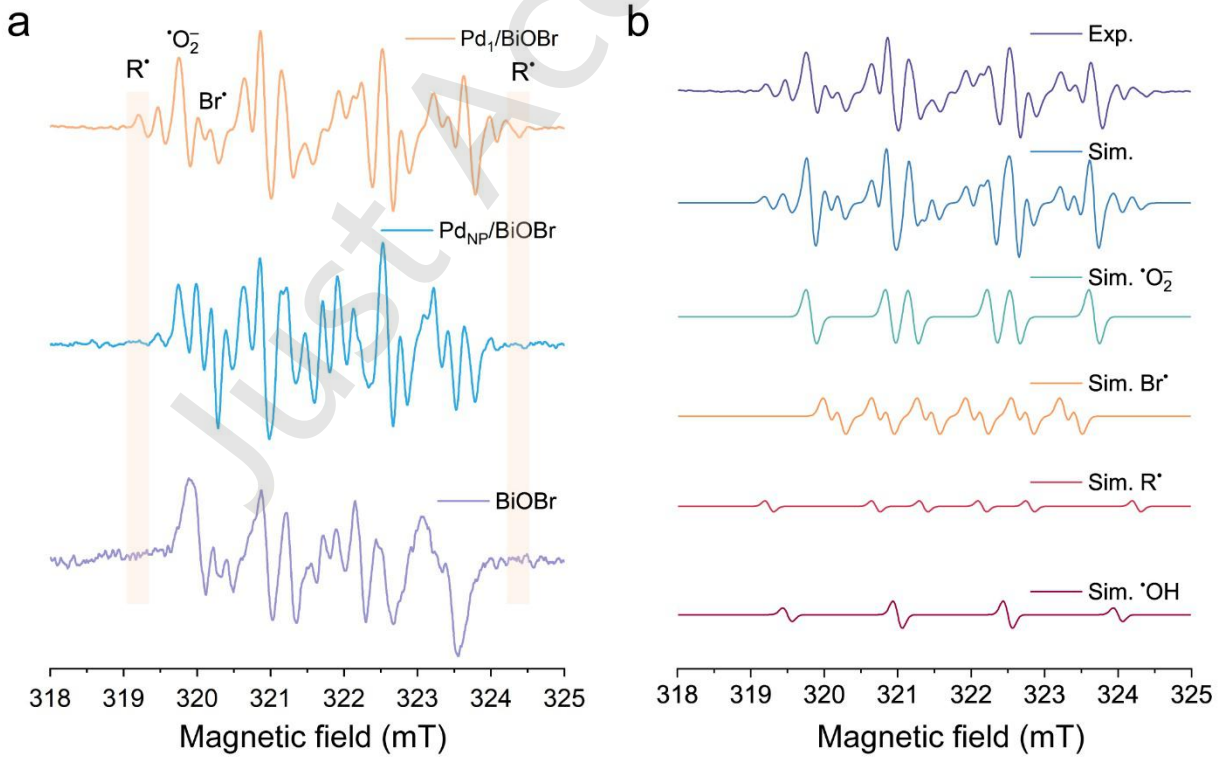


Figure S9 (a) EPR spectra of various samples after 8 minutes of light irradiation; (b) Experimental and fitted EPR spectra of Pd_1/BiOBr after 8 minutes of light irradiation.

Just Accepted

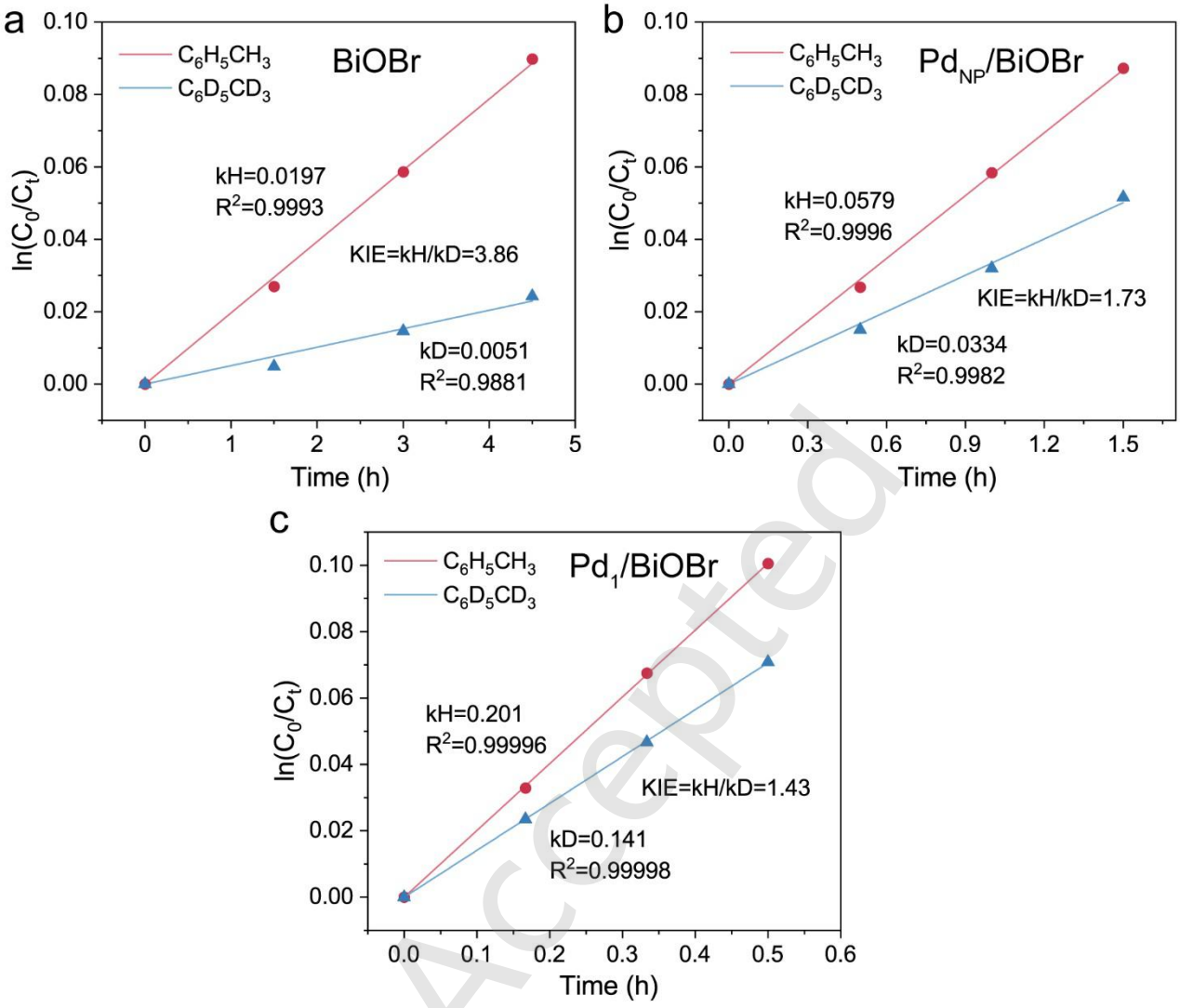


Figure S10 Kinetic profiles of different samples measured with toluene and deuterated toluene as substrates: (a) BiOBr, (b) Pd_{NP}/BiOBr, (c) Pd_1/BiOBr.

Just Accepted

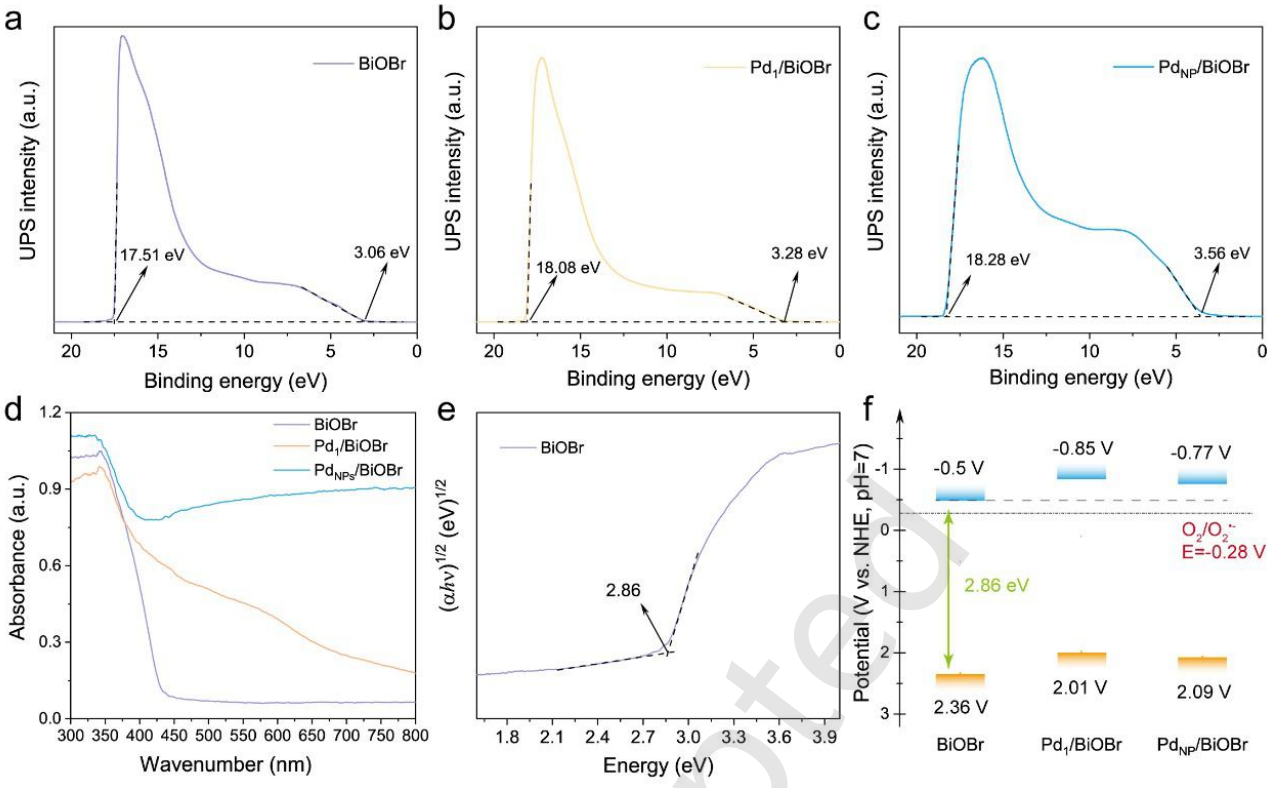


Figure S11 UPS spectra of (a) BiOBr, (b) Pd_1/BiOBr, and (c) Pd_{NP}/BiOBr; (d) UV-vis DRS spectra of the samples; (e) Tauc plot of BiOBr derived from UV-Vis DRS. The extrapolated bandgap value is 2.86 eV. (f) Band structure characterization of the samples.

The electronic structures of the aforementioned samples were characterized using UPS and UV-vis absorption spectroscopy. From the UPS measurements, the valence band level of BiOBr relative to the vacuum level was determined to be 6.8 eV (calculated as 21.22 −17.51 + 3.06) [15], which corresponds to 2.36 eV versus the normal hydrogen electrode (NHE) (Figure S10a). For Pd_1/BiOBr and Pd_{NP}/BiOBr, the valence band potentials were estimated to be 2.01 eV and 2.09 eV vs. NHE, respectively, slightly lower than that of the pristine BiOBr support (Figure S10 b–c). Because only Pd single atoms and nanoparticles were loaded onto the BiOBr nanosheets, the bandgap of the BiOBr supports was not substantially altered.

Accordingly, the UV-vis absorption spectra of Pd_1/BiOBr and Pd_{NP}/BiOBr exhibited no obvious shift in the absorption edge relative to BiOBr (Figure S10 d). However, their optical absorption in the visible region was markedly enhanced, attributed to ligand-to-metal charge transfer [16] and interband transitions of Pd nanoparticles [17], respectively. Further analysis of the BiOBr absorption spectrum yielded a bandgap of 2.86 eV. Combining this with the UPS data, the band structure diagrams of the samples were constructed (Figure S10f). Notably, the conduction band minima (CBM) of Pd_1/BiOBr and Pd_{NP}/BiOBr were upshifted, rendering the photogenerated electrons more negative in potential, which facilitates the reduction of surface molecular oxygen [18].

Just Accepted

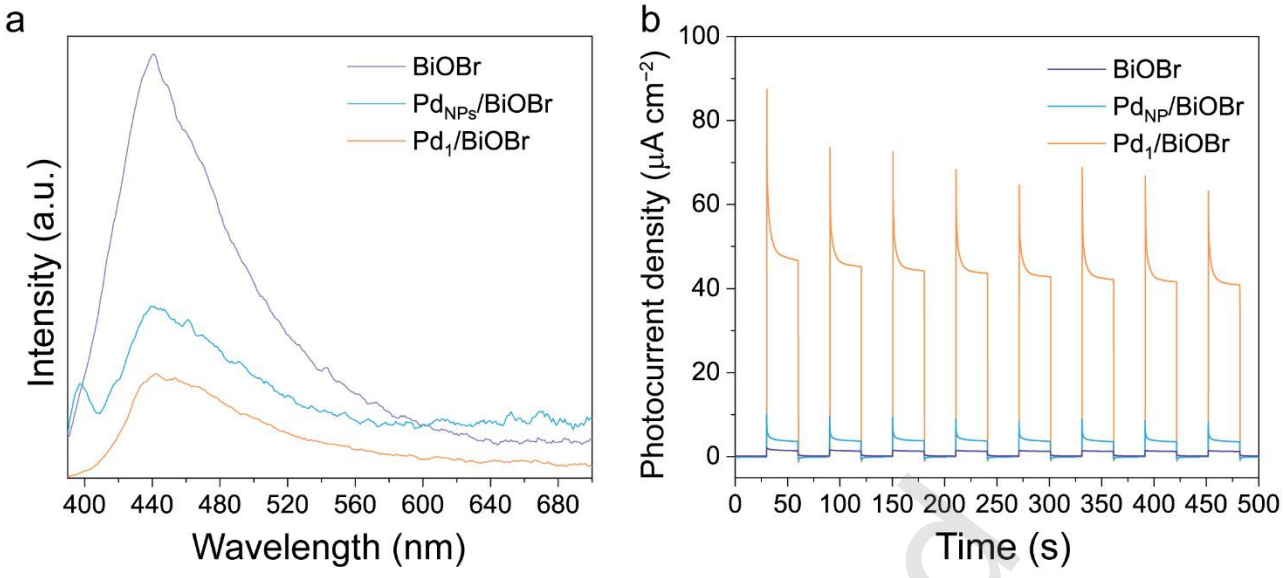


Figure S12 (a) steady-state photoluminescence spectra and (b) photocurrent density plots of the various samples.

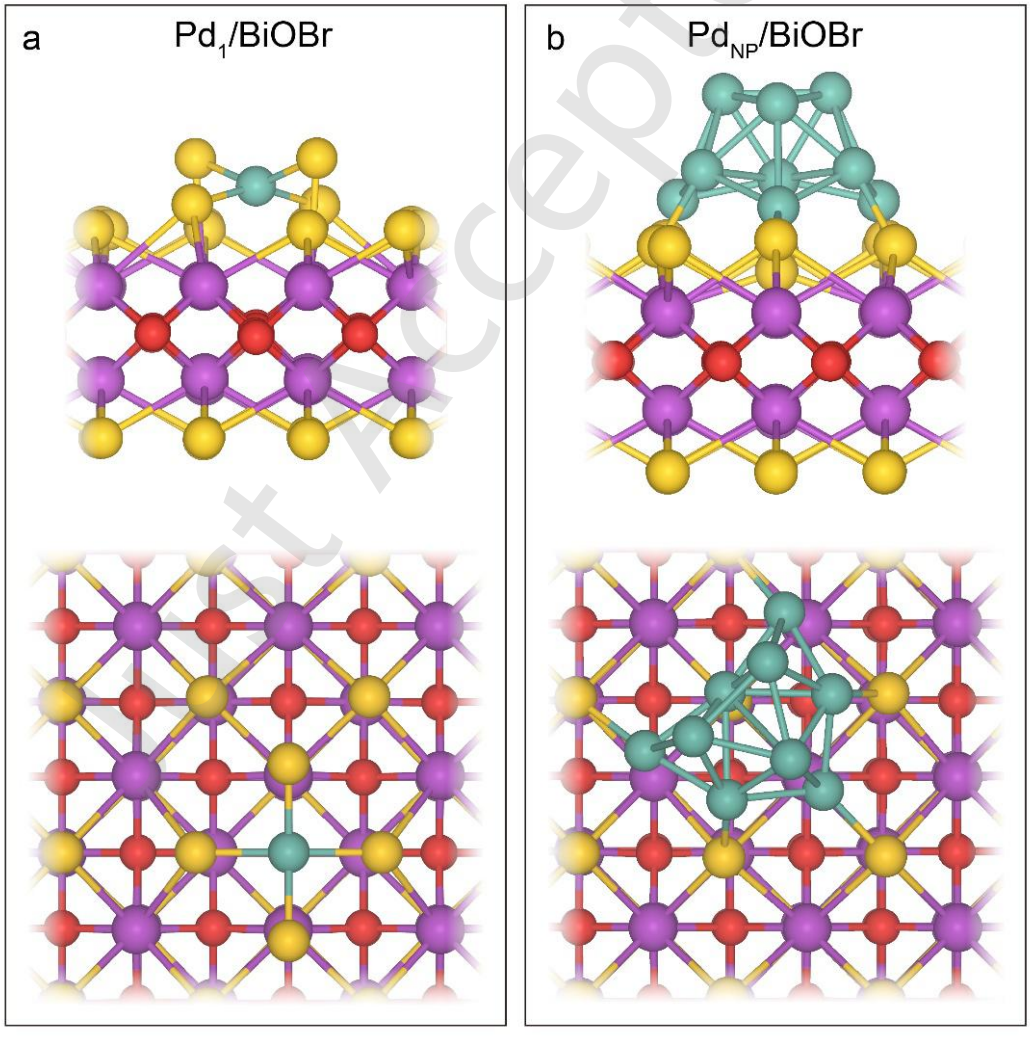


Figure S13 The plots of different views for the optimal structures of Pd_1/BiOBr and Pd_{NP}/BiOBr, respectively. Atom Colors: Bi (purple), Pd (green), Br (yellow), O (red).

Just Accepted

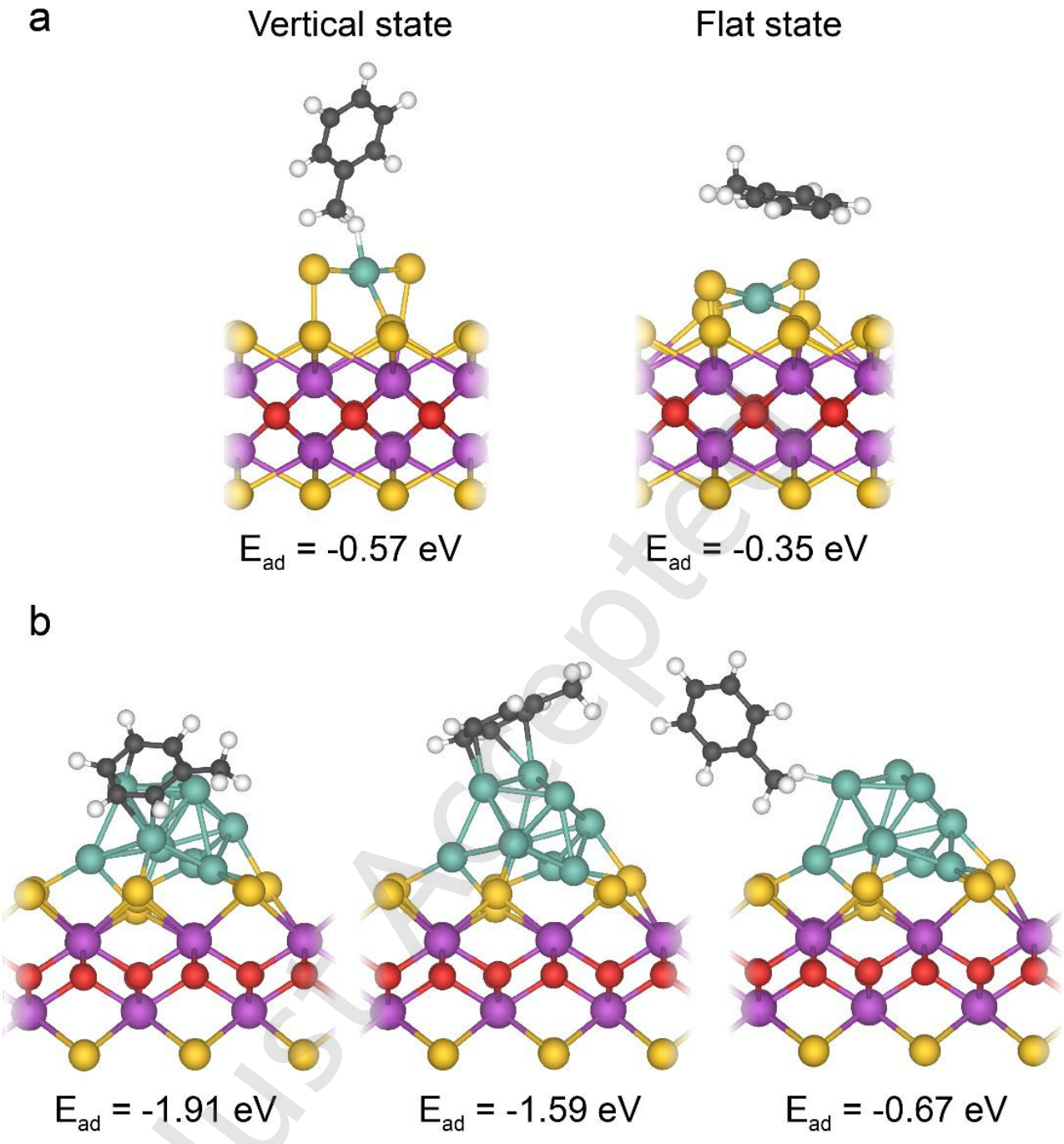


Figure S14 (a) The optimal structures of toluene adsorbed on Pd sites of Pd_1/BiOBr, and E_{ad} refers to the chemisorption energies of toluene. (b) The optimal structures of toluene adsorbed on Pd sites of Pd_{NP}/BiOBr. Atom colors: Bi (purple), Pd (green), Br (yellow), C (gray), O (red), H (white).

Just Accepted

Reference

[1] Cao, X.; Huang, A.; Liang, C.; Chen, H.-C.; Han, T.; Lin, R.; Peng, Q.; Zhuang, Z.; Shen, R.; Chen, H. M.; et al. Engineering Lattice Disorder on a Photocatalyst: Photochromic BiOBr Nanosheets Enhance Activation of Aromatic C–H Bonds via Water Oxidation. *J. Am. Chem. Soc.*, **2022**, *144* (8), 3386–3397.

[2] Li, X.; Wang, T.; Tao, X.; Qiu, G.; Li, C.; Li, B. Interfacial Synergy of Pd Sites and Defective BiOBr for Promoting the Solar-Driven Selective Oxidation of Toluene. *J. Mater. Chem. A*, **2020**, *8* (34), 17657–17669.

[3] Liu, J.; Liu, Y.; Liu, N.; Han, Y.; Zhang, X.; Huang, H.; Lifshitz, Y.; Lee, S. T.; Zhong, J.; Kang, Z. Water Splitting. Metal-Free Efficient Photocatalyst for Stable Visible Water Splitting via a Two-Electron Pathway. *Science*, **2015**, *347* (6225), 970–974.

[4] Kresse, G.; Furthmüller, J. Efficiency of Ab-Initio Total Energy Calculations for Metals and Semiconductors Using a Plane-Wave Basis Set. *Comput. Mater. Sci.*, **1996**, *6* (1), 15–50.

[5] Kresse, G.; Furthmuller, J. Efficient Iterative Schemes for *Ab Initio* Total-Energy Calculations Using a Plane-Wave Basis Set. *Phys. Rev. B Condens. Matter.*, **1996**, *54* (16), 11169–11186.

[6] Kresse, G.; Joubert, D. From Ultrasoft Pseudopotentials to the Projector Augmented-Wave Method. *Phys Rev B*, **1999**, *59* (3), 1758–1775.

[7] Perdew, J. P.; Burke, K.; Ernzerhof, M. Generalized Gradient Approximation Made Simple. *Phys. Rev. Lett.*, **1996**, *77* (18), 3865–3868.

[8] Grimme, S.; Antony, J.; Ehrlich, S.; Krieg, H. A Consistent and Accurate Ab Initio Parametrization of Density Functional Dispersion Correction (DFT-D) for the 94 Elements H-Pu. *J. Chem. Phys.*, **2010**, *132* (15), 154104–154122.

[9] Setyawan, W.; Curtarolo, S. High-Throughput Electronic Band Structure Calculations: Challenges and Tools. *Comput. Mater. Sci.*, **2010**, *49* (2), 299–312.

[10] Henkelman, G.; Uberuaga, B. P.; Jónsson, H. A Climbing Image Nudged Elastic Band Method for Finding Saddle Points and Minimum Energy Paths. *J. Chem. Phys.*, **2000**, *113* (22), 9901–9904.

[11] Henkelman, G.; Jónsson, H. Improved Tangent Estimate in the Nudged Elastic Band Method for Finding Minimum Energy Paths and Saddle Points. *J. Chem. Phys.*, **2000**, *113* (22), 9978–9985.

[12] Wang, V.; Xu, N.; Liu, J.-C.; Tang, G.; Geng, W.-T. VASPKIT: A User-Friendly Interface Facilitating High-Throughput Computing and Analysis Using VASP Code. *Comput. Phys. Commun.*, **2021**, *267*, 108033.

[13] Momma, K.; Izumi, F. VESTA: A Three-Dimensional Visualization System for Electronic and Structural Analysis. *J. Appl. Crystallogr.*, **2008**, *41* (3), 653–658.

[14] Cao, X.; Chen, Z.; Lin, R.; Cheong, W.-C.; Liu, S.; Zhang, J.; Peng, Q.; Chen, C.; Han, T.; Tong, X.; et al. A Photochromic Composite with Enhanced Carrier Separation for the Photocatalytic Activation of Benzylic C–H Bonds in Toluene. *Nat. Catal.*, **2018**, *1* (9), 704–710.

[15] Di, J.; Song, P.; Zhu, C.; Chen, C.; Xiong, J.; Duan, M.; Long, R.; Zhou, W.; Xu, M.; Kang, L.; et al. Strain-Engineering of $Bi_{12}O_{17}Br_2$ Nanotubes for Boosting Photocatalytic CO_2 Reduction. *ACS Materials Letters*, **2020**, *2* (8), 1025–1032.

[16] Creutz, C.; Brunschwig, B. S.; Sutin, N. Interfacial Charge-Transfer Absorption: 3. Application to Semiconductor-Molecule Assemblies. *J. Phys. Chem. B*, **2006**, *110* (50), 25181–25190.

[17] Song, H.; Meng, X.; Wang, Z.; Wang, Z.; Chen, H.; Weng, Y.; Ichihara, F.; Oshikiri, M.; Kako, T.; Ye, J. Visible-Light-Mediated Methane Activation for Steam Methane Reforming under Mild Conditions: A Case Study of Rh/TiO_2 Catalysts. *ACS Catal.*, **2018**, *8* (8), 7556–7565.

[18] Guan, M.; Xiao, C.; Zhang, J.; Fan, S.; An, R.; Cheng, Q.; Xie, J.; Zhou, M.; Ye, B.; Xie, Y. Vacancy Associates Promoting Solar-Driven Photocatalytic Activity of Ultrathin Bismuth Oxychloride Nanosheets. *J. Am. Chem. Soc.*, **2013**, *135* (28), 10411–10417.

Just Accepted